Effect of Edge Shear Flow on Radial Spreading of Ballooning Mode Turbulence

Ayumi TAKANO, Seiya NISHIMURA*,1), Makoto SASAKI2) and Yusuke KOSUGA3)

Department of Electric and Electronic Engineering, Hosei University, Koganei 184-8584, Japan
1) *National Institute for Quantum Science and Technology, Naka 311-0193, Japan*
2) *College of Industrial Technology, Nihon University, Narashino 275-8575, Japan*
3) *Research Institute for Applied Mechanics, Kyushu University, Fukuoka 816-8580, Japan*

(Received 3 October 2023 / Accepted 8 February 2024)

Turbulent transport by the ballooning mode in tokamak plasmas with edge pedestals is simulated using a reduced set of two-fluid equations. In the absence of the equilibrium poloidal flow, global heat transport by the secondary nonlinear evolution of the resistive ballooning mode turbulence is observed. By examining the effect of the edge shear flow, the global heat transport is suppressed to be almost half, if the edge shear flow is strong enough. A detailed analysis on the radial profile and the poloidal spectrum of the heat flux is newly performed. It is revealed that such confinement improvement is caused by the suppression of the formation of streamer structures that lead to the strong convective heat transport.

Keywords: tokamak plasma, resistive ballooning mode, nonlinear evolution, turbulence spreading, shear flow

DOI: 10.1585/pfr.19.1403016

1. Introduction

For magnetically confinement fusion plasmas such as tokamak plasmas, it is an important issue to understand and control magnetohydrodynamic (MHD) turbulence. In particular, the edge localized mode (ELM) due to the ballooning mode has been observed in the edge region of tokamaks, causing partial collapse of the pressure profile and large heat load on the divertor [1]. In addition, a recent experimental observation shows that the radially elongated flow, i.e. the streamer, generated by the ballooning mode turbulence plays an important role in the triggering of the type-III ELM [2].

Theoretical and numerical studies on the ballooning mode are mainly classified into the following four categories. First, the stability analysis of the ballooning mode has been conducted taking into account realistic poloidal geometries and various equilibrium profiles [3–5]. In this line of research, it has been considered that coupling of the peeling mode, driven by the edge bootstrap current, and the ballooning mode is essential for the ELM accompanying the largest collapse, so-called type-I ELM [6]. Second, nonlinear simulations of the ballooning mode have been performed to understand nonlinear evolution and saturation mechanisms of the ballooning mode turbulence [7–9]. Third, in order to reproduce the repetitive burst transport due to the ELM, nonlinear simulations of the ballooning mode turbulence in the presence of the heat source have been performed [10, 11]. Fourth, associated with the interaction between the ballooning mode turbulence and magnetic islands, studies have been carried out to examine the physical mechanism of how bursty heat transport by the ELM is mitigated or suppressed by the so-called resonant magnetic perturbation (RMP) [12–15].

In this study, we focus on the nonlinear evolution of the resistive ballooning mode turbulence in the absence of the heat source and the peeling mode. In the preceding works, it has been shown that the linear instability of the ballooning mode occurs locally, whereas the ballooning mode turbulence spreads globally in the radial direction [7–9]. Originally, the turbulence spreading in the radial direction has been studied in detail in terms of the drift wave turbulence [16–18]. In the turbulence spreading, the pressure gradient and the turbulence amplitude move radially inward are simultaneously observed, which is also called the front propagation. However, for the ballooning mode turbulence, the detailed mechanism of the turbulence spreading is not fully understood. In particular, it has been pointed out that the loss of the stored energy due to the ballooning mode turbulence is suppressed to a low level, when the edge poloidal flow exists [8, 9]. In order to clarify such a reduction mechanism, we newly introduce an analyzing method of the radial profile and the mode number spectrum of the heat flux accompanying the ballooning mode turbulence.

Remainder of this paper is organized as follows. In Sec. 2, the reduced two-fluid model of tokamak plasmas is introduced. We show a law of the conservation of energy and derive a time evolution equation of the stored energy. In addition, parameters and equilibrium profiles used in nonlinear simulations are also shown. The nonlin-

* *Corresponding author's e-mail: nishimura.seiya@qst.go.jp*

ear simulation results and analyses on them are shown in Sec. 3. The reduction of the stored energy loss due to the edge poloidal shear flow is observed. The heat flux due to the ballooning mode turbulence is analyzed, and the reduction of the convective heat flux by the shear flow is found to be essential. Then, time evolution of the radial profile and the mode number spectrum of the convective heat flux are analyzed. It is concluded that the edge shear flow affects the nonlinear characteristics of the ballooning mode turbulence, which avoids both the radial turbulence spreading and the global heat transport. Section 4 is devoted for a summary.

2. Simulation Model

2.1 Reduced two-fluid model

Our simulation model is based on the conventional Hazeltine's reduced two-fluid model [19], where tokamak plasmas with large aspect ratios are modeled by cylindrical plasmas with effective toroidal curvatures. In the model, a quasi-neutral condition between ion and electron densities is considered, and the cold ion approximation is used. For simplicity, we neglect the ion diamagnetic drift, the ion parallel velocity, and the electron inertia. The vorticity equation, the generalized Ohm's law, and the pressure evolution equation (the electron continuity equation for constant temperature) are given by

$$\frac{dU}{dt} = \nabla_\parallel j_\parallel - [x, p] + \mu \nabla_\perp^2 U, \tag{1}$$

$$\frac{\partial A_\parallel}{\partial t} = -\nabla_\parallel(\phi - \delta p) - \eta_\parallel(j_\parallel - j_{\parallel 0}), \tag{2}$$

$$\frac{dp}{dt} = 2\delta\beta\nabla_\parallel j_\parallel + 2\beta[x, \phi - \delta p] + \chi\nabla_\perp^2 p, \tag{3}$$

respectively. The definition of U and the Ampère's law are given by

$$U = \nabla_\perp^2 \phi, \tag{4}$$

$$j_\parallel = -\nabla_\perp^2 A_\parallel, \tag{5}$$

respectively. The operators are defined by

$$\frac{d}{dt} = \frac{\partial}{\partial t} + [\phi,\ ], \tag{6}$$

$$\nabla_\parallel = \frac{\partial}{\partial z} - [A_\parallel,\ ], \tag{7}$$

$$[f, g] = \hat{\boldsymbol{z}} \cdot \nabla_\perp f \times \nabla_\perp g, \tag{8}$$

$$\nabla_\perp = \hat{\boldsymbol{r}}\frac{\partial}{\partial r} + \hat{\boldsymbol{\theta}}\frac{1}{r}\frac{\partial}{\partial \theta}, \tag{9}$$

where f and g are arbitrary variables.

In the cylindrical coordinates (r, θ, z), the coordinate variables $\{r, \theta, z\}$ are the minor radial position, the poloidal phase angle, and the toroidal position, respectively, and $\{\hat{\boldsymbol{r}}, \hat{\boldsymbol{\theta}}, \hat{\boldsymbol{z}}\}$ are unit vectors. The variables $\{U, \phi, A_\parallel, j_\parallel, p\}$ denote the vorticity, the electrostatic potential, the parallel component of the vector potential, the parallel current, and the electron pressure, respectively, and $j_{\parallel 0}$ is the equilibrium parallel current. The transport coefficient $\{\mu, \eta_\parallel, \chi\}$ denote the perpendicular momentum diffusivity, the parallel resistivity, and the perpendicular thermal diffusivity, respectively. The major radial position measured from the plasma center is defined by $x = r\cos\theta$, and the effective curvature of the toroidal magnetic field field is given by $\boldsymbol{\kappa}_0 = -\nabla_\perp x$.

The time and length are normalized as $t/\tau_\mathrm{A} \to t$, $r/a \to r$, and $z/R_0 \to z$, where $\tau_\mathrm{A} = R_0/v_\mathrm{A}$, v_A is the Alfvén velocity, a is the minor radius, and R_0 is the major radius. The normalized parameters are defined as follows: β is the ratio between the kinetic pressure and the magnetic pressure measured at the plasma center, and δ is the ion inertia length normalized by $2a$. The other variables and operators are normalized as follows: $a\nabla_\perp \to \nabla_\perp$, $R_0\nabla_\parallel \to \nabla_\parallel$, $R_0\boldsymbol{\kappa}_0 \to \boldsymbol{\kappa}_0$, $(c\tau_\mathrm{A}/a^2 B_0)\phi \to \phi$, $A_\parallel/\epsilon a B_0 \to A_\parallel$, $(4\pi R_0/cB_0)j_\parallel \to j_\parallel$, $(8\pi/\epsilon B_0^2)p \to p$, $(\tau_\mathrm{A}/a^2)\mu \to \mu$, $(c^2\tau_\mathrm{A}/4\pi a^2)\eta_\parallel \to \eta_\parallel$, and $(\tau_\mathrm{A}/a^2)\chi \to \chi$, where c is the velocity of light, $\epsilon = a/R_0$ is the inverse aspect ratio of torus, and B_0 is the representative magnitude of the toroidal magnetic field.

2.2 Energy conservation and heat flux

In the cylindrical coordinates, we assume that an arbitrary variable $f(r, \theta, z, t)$ can be expanded into complex Fourier series as

$$\begin{aligned} f(r, \theta, z, t) &= f_0(r) + \tilde{f}(r, \theta, z, t) \\ &= f_0(r) + \sum_{m,n} \tilde{f}_{m,n}(r, t)\exp\left[i(m\theta - nz)\right], \end{aligned} \tag{10}$$

where $\{m, n\}$ are the poloidal and toroidal mode numbers, respectively. Hereafter, variables with the subscript 0 denote equilibrium quantities, and those with the tilde denote perturbation quantities.

In our preliminary study, it has been observed that numerical instability occurs around $r = 0$ when a finite value of δ is considered. In order to avoid such instability, we limit the domain of the r as $r_0 \le r \le 1$, where $r_0 = 0.1$ is used in this study. The boundary conditions for the perturbation amplitudes are given such that $\tilde{f}_{m,n}(r_0, t) = \tilde{f}_{m,n}(1, t) = 0$ for $(m, n) \neq (0, 0)$ and $\partial_r \tilde{f}_{0,0}|_{r=r_0} = \tilde{f}_{0,0}(1, t) = 0$.

Then, we write down Eqs. (1)-(3) for the (m, n) component of the complex Fourier amplitude as

$$\begin{aligned} \frac{\partial}{\partial t}\tilde{U}_{m,n} =& -ik_\theta\phi_0'\tilde{U}_{m,n} + ik_\theta U_0'\tilde{\phi}_{m,n} - \left[\tilde{\phi}, \tilde{U}\right]_{m,n} \\ &+ ik_\parallel\tilde{j}_{\parallel m,n} + ik_\theta j_{\parallel 0}'\tilde{A}_{\parallel m,n} - \left[\tilde{A}_\parallel, \tilde{j}_\parallel\right]_{m,n} \\ &- [x, \tilde{p}]_{m,n} + \mu\left(\nabla_\perp^2\tilde{U}\right)_{m,n}, \end{aligned} \tag{11}$$

$$\begin{aligned} \frac{\partial}{\partial t}\tilde{A}_{\parallel m,n} =& -ik_\parallel\tilde{\phi}_{m,n} - ik_\theta\phi_0'\tilde{A}_{\parallel m,n} + \left[\tilde{A}_\parallel, \tilde{\phi}\right]_{m,n} \\ &+ i\delta k_\parallel\tilde{p}_{m,n} + i\delta k_\theta p_0'\tilde{A}_{\parallel m,n} - \delta\left[\tilde{A}_\parallel, \tilde{p}\right]_{m,n} \\ &- \eta_\parallel\tilde{j}_{\parallel m,n}, \end{aligned} \tag{12}$$

$$\frac{\partial}{\partial t}\tilde{p}_{m,n} = -ik_\theta \phi_0' \tilde{p}_{m,n} + ik_\theta p_0' \tilde{\phi}_{m,n} - \left[\tilde{\phi}, \tilde{p}\right]_{m,n} + 2\delta\beta\left(ik_\parallel \tilde{j}_{\parallel m,n} + ik_\theta j_{\parallel 0}' \tilde{A}_{\parallel m,n} - \left[\tilde{A}_\parallel, \tilde{j}_\parallel\right]_{m,n}\right) + 2\beta\left[x, \tilde{\phi} - \delta\tilde{p}\right]_{m,n} + \chi\left(\nabla_\perp^2 \tilde{p}\right)_{m,n}, \quad (13)$$

where $k_\theta = m/r$, $k_\parallel = m/q - n$, q is the safety factor ($1/q = -(1/r)(dA_{\parallel 0}/dr)$ in our normalization), the prime indicate the radial derivative, and $(\nabla_\perp^2 \tilde{f})_{m,n} = (1/r)\partial_r(r\partial_r \tilde{f}_{m,n}) - k_\theta^2 \tilde{f}_{m,n}$.

The energy conservation law of Eqs. (1)-(3) in terms of the complex Fourier amplitude is given by

$$\frac{dE}{dt} = L, \quad (14)$$

with

$$E = E_\phi + E_{A_\parallel} + E_p, \quad (15)$$

$$L = S_{\phi_0'} + S_{j_{\parallel 0}'} + S_{p_0'} + S_\mu + S_{\eta_\parallel} + S_\chi, \quad (16)$$

where the components of each perturbation energy are defined by

$$E_\phi = \sum_{m,n} E_\phi^{m,n} = \sum_{m,n} \frac{1}{2}\int_{r_0}^1 \left|\left(\nabla_\perp \tilde{\phi}\right)_{m,n}\right|^2 rdr, \quad (17)$$

$$E_{A_\parallel} = \sum_{m,n} E_{A_\parallel}^{m,n} = \sum_{m,n} \frac{1}{2}\int_{r_0}^1 \left|\left(\nabla_\perp \tilde{A}_\parallel\right)_{m,n}\right|^2 rdr, \quad (18)$$

$$E_p = \sum_{m,n} E_p^{m,n} = \sum_{m,n} \frac{1}{4\beta}\int_{r_0}^1 \left|\tilde{p}_{m,n}\right|^2 rdr, \quad (19)$$

with $|(\nabla_\perp \tilde{f})_{m,n}|^2 = |\partial \tilde{f}_{m,n}/\partial r|^2 + k_\theta^2 |\tilde{f}_{m,n}|^2$ for arbitrary $\tilde{f}$. In addition, $\{S_{\phi_0'}, S_{j_{\parallel 0}'}, S_{p_0'}\}$ are the energy sources associated with radial gradients of the the electrostatic potential, the parallel current, and the pressure, respectively, involved in the linear terms in Eqs. (11)-(13), and $\{S_\mu, S_{\eta_\parallel}, S_\chi\}$ are the energy sinks associated with each transport coefficient. Note that contributions of various nonlinear terms and quasilinear terms associated with the toroidal curvature are cancelled out each other in the final form of the energy conservation law. For later use, we define the pressure energy perturbation summed over n as

$$E_p^m = \sum_n E_p^{m,n}. \quad (20)$$

In this study, the stored energy is defined by

$$W = 4\pi^2 \int_{r_0}^r (p_0 + \tilde{p}_{0,0})\, rdr = W_0 - \Delta W, \quad (21)$$

where $W_0 = 4\pi^2 \int_{r_0}^r p_0 rdr$ is the initial stored energy and $\Delta W = -4\pi^2 \int_{r_0}^r \tilde{p}_{0,0} rdr$ is the loss of the stored energy. In order to derive the time evolution of the loss of the stored energy, we write down the $(m,n) = (0,0)$ component of Eq. (13) as

$$\frac{\partial}{\partial t}\tilde{p}_{0,0} = -\left[\tilde{\phi}, \tilde{p}\right]_{0,0} - 2\delta\beta\left[\tilde{A}_\parallel, \tilde{j}_\parallel\right]_{0,0} + 2\beta\left[x, \tilde{\phi} - \delta\tilde{p}\right]_{0,0} + \chi\left(\nabla_\perp^2 \tilde{p}\right)_{0,0}. \quad (22)$$

Operating $\int_{r_0}^r dr\, r$ to Eq. (22) gives

$$-\frac{1}{4\pi^2}\frac{\partial}{\partial t}\Delta W = h_{\rm conv} + h_{\rm EM} + h_{\rm curv} + h_{\rm diff}, \quad (23)$$

with

$$h_{\rm conv} = -\int_{r_0}^r \left[\tilde{\phi}, \tilde{p}\right]_{0,0} rdr, \quad (24)$$

$$h_{\rm EM} = -2\delta\beta \int_{r_0}^r \left[\tilde{A}_\parallel, \tilde{j}_\parallel\right]_{0,0} rdr, \quad (25)$$

$$h_{\rm curv} = 2\beta \int_{r_0}^r \left[x, \tilde{\phi} - \delta\tilde{p}\right]_{0,0} rdr, \quad (26)$$

$$h_{\rm diff} = \chi \int_{r_0}^r \left(\nabla_\perp^2 \tilde{p}\right)_{0,0} rdr, \quad (27)$$

where $\{h_{\rm conv}, h_{\rm EM}, h_{\rm curv}, h_{\rm diff}\}$ are the heat fluxes associated with the convection, the electromagnetic perturbation, the curvature, and the thermal diffusion, respectively.

For later use, we also derive an expression for extracting the modes that drive the convective heat transport. First, $\left[\tilde{\phi}, \tilde{p}\right]_{0,0}$ in Eq. (24) can be rewritten as

$$\left[\tilde{\phi}, \tilde{p}\right]_{0,0} = -\sum_{m,n} ik_\theta \frac{\partial}{\partial r}\left(\tilde{\phi}_{m,n}\tilde{p}_{m,n}^*\right), \quad (28)$$

where $\tilde{p}_{-m,-n} = \tilde{p}_{m,n}^*$ is used, and f^* is the complex conjugate of arbitrary f. Substituting Eq. (28) into Eq. (24) gives

$$h_{\rm conv} = \sum_{m,n} h_{\rm conv}^{m,n}, \quad (29)$$

with

$$h_{\rm conv}^{m,n} = im\tilde{\phi}_{m,n}\tilde{p}_{m,n}^*. \quad (30)$$

Summing over n and considering the complex conjugation property, the convective heat transport is also separated as

$$h_{\rm conv} = \sum_{m>0} H_{\rm conv}^m, \quad (31)$$

with

$$H_{\rm conv}^m = \sum_n \left(h_{\rm conv}^{m,n} + h_{\rm conv}^{-m,-n}\right) = \sum_n 2{\rm Re}\left(im\tilde{\phi}_{m,n}\tilde{p}_{m,n}^*\right). \quad (32)$$

2.3 Simulation condition

In this study, the equilibrium profiles are given by

$$q = 2 + 2r^2, \quad (33)$$

$$p_0 = \frac{\beta}{2\epsilon}\left(1 - r^2\right)\left[1 - \tanh\left(\frac{r - r_{\rm s}}{d}\right)\right], \quad (34)$$

$$\phi_0 = \alpha\delta p_0, \quad (35)$$

where $\{r_{\rm s}, d, \alpha\}$ are arbitrary. The profile of $j_{\parallel 0}$ is determined by the cylindrical MHD equilibrium in our normalization:

$$j_\theta B_z - \epsilon^2 j_{\parallel 0} B_\theta = \frac{\epsilon}{2} p_0', \quad (36)$$

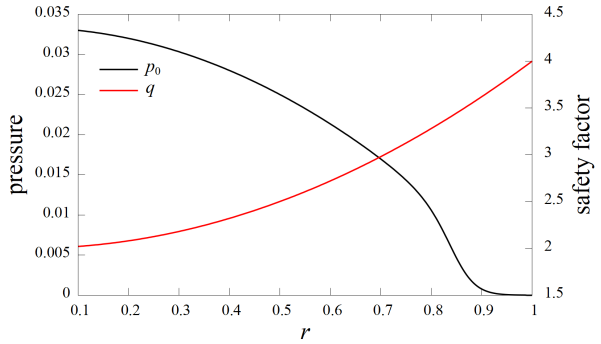

Fig. 1 Radial profile of the equilibrium pressure p_0 and safety factor q.

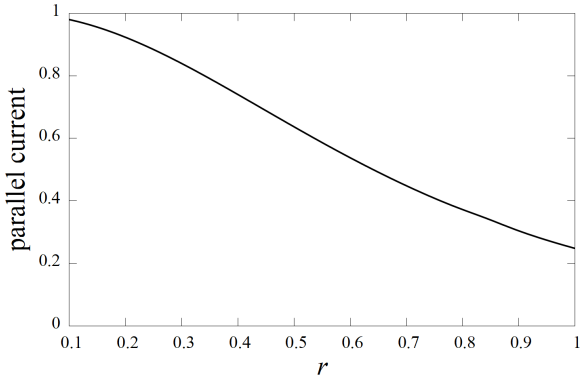

Fig. 2 Radial profile of the equilibrium parallel current $j_{\parallel 0}$.

where $j_\theta = -(dB_z/dr)$, $j_{\parallel 0} = (1/r)d(rB_\theta)/dr$, and $B_z = qB_\theta/r$. Then, the determination of $j_{\parallel 0}$ is reduced to solve the following differential equation for B_θ^2:

$$\frac{dB_\theta^2}{dr} = -\frac{2}{(q^2/r^2)+\epsilon^2}\left(\frac{\epsilon p_0'}{2} + fB_\theta^2\right), \tag{37}$$

$$f = \frac{d}{dr}\left(\frac{q^2}{2r^2}\right) + \frac{\epsilon^2}{r}. \tag{38}$$

In the following simulations, the parameters are chosen such that $\beta = 0.01$, $\delta = 0.04$, $\epsilon = 0.3$, $\mu = 10^{-5}$, $\eta_\parallel = 10^{-5}$, $\chi = 10^{-5}$, $r_s = 0.85$, $r_0 = 0.1$, $d = 0.05$. The time step is $\Delta t = 0.01$, and the radial resolution is $\Delta r = (1 - r_0)/256$, and Fourier modes with $-40 \le m \le 40$ and $-20 \le n \le 20$ are solved.

Figure 1 shows the radial profile of the equilibrium pressure and the safety factor. There exists a sharp radial gradient of the pressure around $r = 0.85$, where the resistive ballooning mode is initially destabilized. Similarly, Fig. 2 shows the radial profile of the equilibrium parallel current, which is the solution of the cylindrical MHD equilibrium. The poloidal E × B flow velocity is given by

$$v_E = v_{E0} + \tilde{v}_{E0,0}, \tag{39}$$

where $v_{E0} = \phi_0'$ is the equilibrium poloidal E × B flow velocity and $\tilde{v}_{E0,0} = \tilde{\phi}_{0,0}'$ represents the modification of the

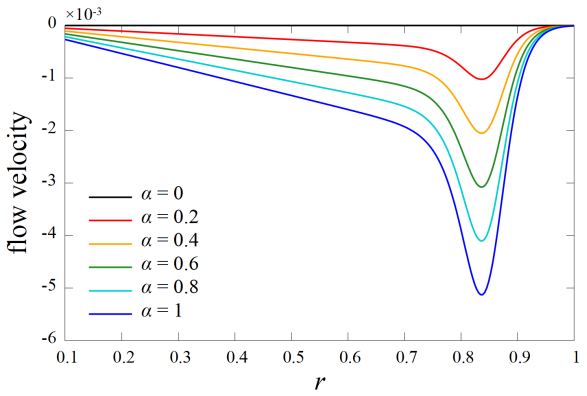

Fig. 3 Radial profile of the equilibrium poloidal flow velocity v_{E0} for $\alpha = 0, 0.2, 0.4, 0.6, 0.8$, and 1.

poloidal flow velocity due to nonlinear effects. In order to study the effect of the edge shear flow on the evolution of the ballooning mode turbulence, we conduct the parameter survey for different values of α in Eq. (35). Figure 3 shows the radial profile of the equilibrium poloidal E × B flow velocity. It is observed that sharp radial gradients of the flow velocity are formed in the edge region. In addition, the absolute value of the velocity for the case with $\alpha = 1$ agrees with that of the electron diamagnetic drift velocity defined by $v_* = -\delta p_0'$.

3. Simulation Results and Analyses

In the following, simulation results of the nonlinear evolution of the resistive ballooning mode turbulence are shown, and effects of the edge shear flow on the radial turbulence spreading are analyzed in detail.

Figure 4 shows the color contours of the pressure perturbation in the poloidal cross section in the *absence* of the edge shear flow ($\alpha = 0$) at different times, where Z is the vertical position normalized by the minor radius. The ballooning mode with $m \sim 30$ is in the linear growth phase at $t = 100$ (Fig. 4 (i)), and the mode is excited near the radial position of the peak of the equilibrium pressure gradient $r = 0.83$. It is observed that the mode is in the nonlinear evolution phase at $t = 150$ (Fig. 4 (ii)), where the ballooning structure collapses due to the energy cascade of the unstable modes and the transition to a turbulent state with a complex structure. In more nonlinearly developed phases at $t = 400$ and $t = 600$ (Figs. 4 (iii) and 4 (iv), respectively), the secondary turbulence spreading occurs in the radial direction, where intermediate-scale structures with $m \sim 10$ modes are formed.

Here, the intermediate-scale structures with $m \sim 10$ observed in Figs. 4 (iii) and 4 (iv) are considered to be so-called streamer structures. The group of the streamers has the ballooning structure, where multiple poloidal/toroidal modes are combined. It is confirmed that $m \sim 10$ modes in the initial growing phase as Fig. 4 (i) are marginally stable. Therefore, the development of the streamers is a nonlinear

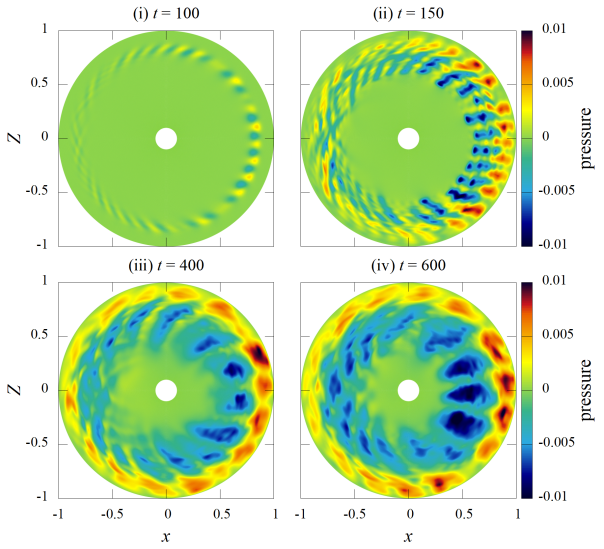

Fig. 4 Color contours of the pressure perturbation in the poloidal cross section in the *absence* of the edge shear flow ($\alpha = 0$ in Fig. 3) at (i) $t = 100$, (ii) $t = 150$, (iii) $t = 400$, and (iv) $t = 600$.

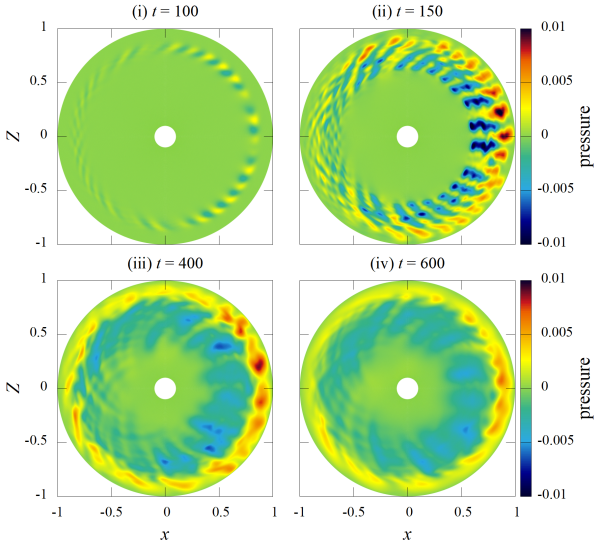

Fig. 5 Color contours of the pressure perturbation in the poloidal cross section in the *presence* of the strong edge shear flow ($\alpha = 1$ in Fig. 3) at (i) $t = 100$, (ii) $t = 150$, (iii) $t = 400$, and (iv) $t = 600$.

phenomenon and occurs simultaneously with the deformation of the pressure profile. Since the streamer structure is less susceptible to the diffusion damping compared with the micromodes, its radially extending structure is suitable for driving global heat transport. As shown below, it is considered that the system spontaneously generates such structures for efficient heat transport.

Figure 5 shows the color contours of the pressure perturbation in the poloidal cross section in the *presence* of the strong edge shear flow ($\alpha = 1$) at different times. Even

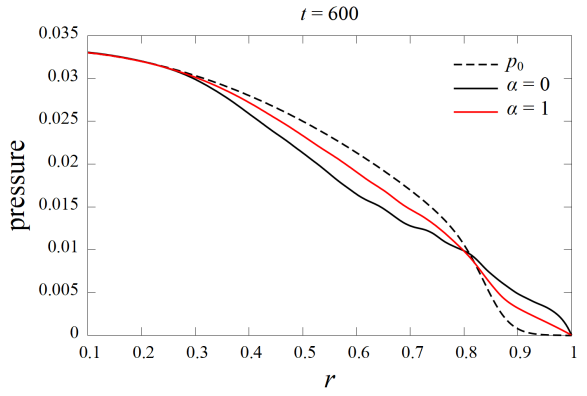

Fig. 6 Radial profiles of the pressure $p_0 + \tilde{p}_{0,0}$ for $\alpha = 0$ and $\alpha = 1$.

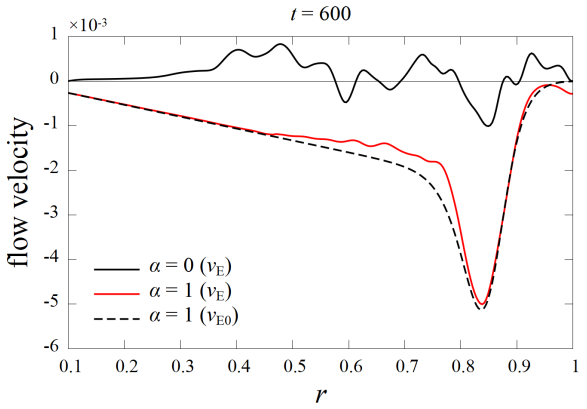

Fig. 7 Radial profiles of the poloidal flow velocity $v_E = v_{E0} + \tilde{v}_{E0,0}$ for $\alpha = 0$ and $\alpha = 1$, and v_{E0} for $\alpha = 1$.

in the presence of the strong edge shear flow, similar to Fig. 4, the ballooning structure at $t = 100$ (Fig. 5 (i)) and the transition to the turbulent state at $t = 150$ (Fig. 5 (ii)) are also observed. On the other hand, in more nonlinearly developed phases at $t = 400$ and $t = 600$ (Figs. 5 (iii) and 5 (iv), respectively), the secondary turbulence spreading as observed in Fig. 4 becomes very weak, and the fluctuations are mainly localized in the edge region. Therefore, in our parameter regime, it is found that the edge shear flow does not strongly affect the transition process of the ballooning mode to the turbulent state, but tends to suppress the radial spreading of the turbulence.

Figure 6 shows the radial profile of the pressure $p_0 + \tilde{p}_{0,0}$ at $t = 600$. Compared with the initial state p_0, it is observed that the pressure decreases in the inner region and increases in the outer region, caused by the global turbulent transport. Comparing the cases of $\alpha = 0$ and $\alpha = 1$, such global transport tends to be reduced by the edge shear flow, which is caused by the suppression of the radial turbulence spreading. Corresponding to Fig. 6, Fig. 7 shows the radial profile of the poloidal flow velocity $v_{E0} + \tilde{v}_{E0,0}$ at $t = 600$. For the case with $\alpha = 0$, the poloidal flow is formed even in the core region, which is caused by the ra-

dial turbulence spreading. On the other hand, for the case with $\alpha = 1$, deformation of the poloidal flow profile is suppressed. Therefore, the strong edge shear flow is found to have reduction effects of the radially global heat and momentum transport.

Figure 8 shows the time evolution of the energy loss rate for different values of α. Here, from Eq. (21), the energy loss rate is defined as follows:

$$\eta_{\rm loss} = \left.\frac{\Delta W}{W_0}\right|_{r=0.83}, \tag{40}$$

where $r = 0.83$ is the radial position of the peak of the equilibrium pressure gradient. Since the linear growth rate of the ballooning mode is high compared with the shearing rate of the edge shear flow in our parameter regime, the energy loss rate is not sensitive to the value of α in the linear regime $0 \lesssim t \lesssim 150$. In the first nonlinear saturation phase, $150 \lesssim t \lesssim 250$, the energy loss rate weakly decreases as the value of α increases. In the subsequent nonlinear evolution phase, $250 \lesssim t$, the energy loss rate strongly depends on the value of α. In particular, the energy loss rate for $\alpha = 1$ is roughly half of that for $\alpha = 0$. In addition, from comparison of the small α cases ($\delta = 0.04$) with the $\delta = 0$ case ($v_* = 0$ and $v_{\rm E0} = 0$), it is observed that the electron diamagnetic effect strongly enhances the energy loss in the nonlinear phase. This implies that the electron diamagnetic effect plays an important role in the formation of the streamers.

Here, we consider the suppression mechanism of the streamer structures by the edge shear flow. The time required for the streamer to extend globally in the radial direction (for example, at least, radial length 0.5) is defined as the characteristic time of the streamer $\tau_{\rm stream}$. From Figs. 4 (iii) and 4 (iv), we can estimate $\tau_{\rm stream} \sim 200$. If the shear flow sufficiently twists the streamer in the poloidal direction during the time that the streamer extends in the radial direction, it is considered that the development of the streamer can be suppressed. The length of the twist in the poloidal direction is $r\Delta\theta$, where $\Delta\theta$ is the typical twist angle. Considering that $\Delta\theta$ is the angle that sufficiently twists the $m \sim 10$ mode, that is, the angle that mixes the phases of the neighboring streamers, gives $\Delta\theta = 2\pi/m \sim \pi/5$. Therefore, the characteristic time of twisting due to the shear flow is calculated as follows:

$$\tau_{\rm E0} = \left.\frac{r\Delta\theta}{|v_{\rm E0}|}\right|_{r=0.83} \sim \frac{100}{\alpha}. \tag{41}$$

On the time scales longer than $\tau_{\rm E0}$, it becomes difficult to produce structures cross the edge shear flow. This is consistent the simulation results, Figs. 4, 5 and 8, that $\alpha \sim 0.5$ is sufficient to prevent the formation of the streamer structures. Therefore, it is found that the strong edge shear flow suppresses the development of the streamer structures in the ballooning mode turbulence.

In order to understand the detailed physical mechanism of the reduction of the energy loss rate due to the edge shear flow in Fig. 8, we separate the heat flux into contributions of the convection, the electromagnetic perturbation, the curvature, and the thermal diffusion as shown in the right-hand side of Eq. (23). Figure 9 shows the radial profiles of the decomposed heat fluxes. In the absence of the edge shear flow (Fig. 9 (a)), it is observed that the contribution of the convection is dominant. This result indicates that the radial turbulence spreading is mainly caused by the convective energy transport. On the other hand, the contribution of the convection becomes drastically small in the presence of the strong edge shear flow (Fig. 9 (b)), which

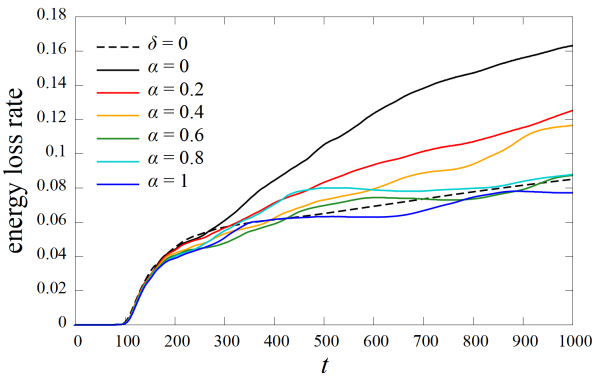

Fig. 8 Time evolution of the energy loss rate for $\alpha = 0, 0.2, 0.4, 0.6, 0.8$, and 1. The case with $\delta = 0$ is also shown as a reference.

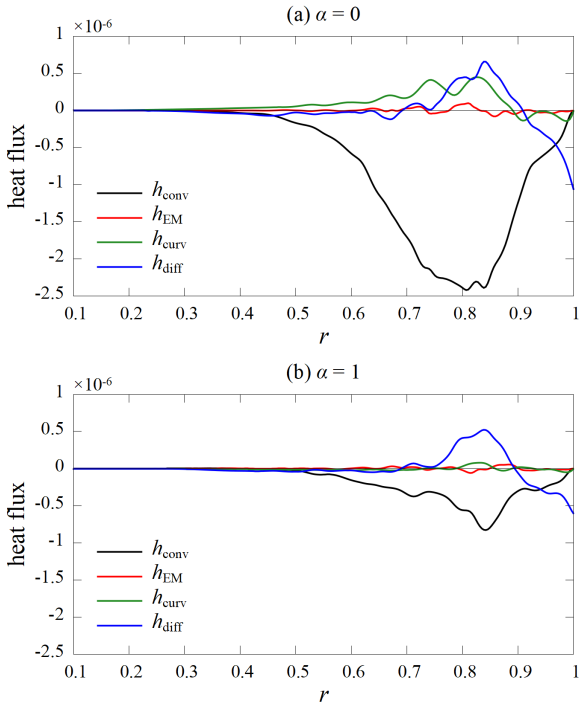

Fig. 9 Radial profiles of the heat fluxes associated with the convection $h_{\rm conv}$, the electromagnetic perturbation $h_{\rm EM}$, the curvature $h_{\rm curv}$, and the thermal diffusion $h_{\rm diff}$ for (a) $\alpha = 0$ and (b) $\alpha = 1$ at $t = 400$.

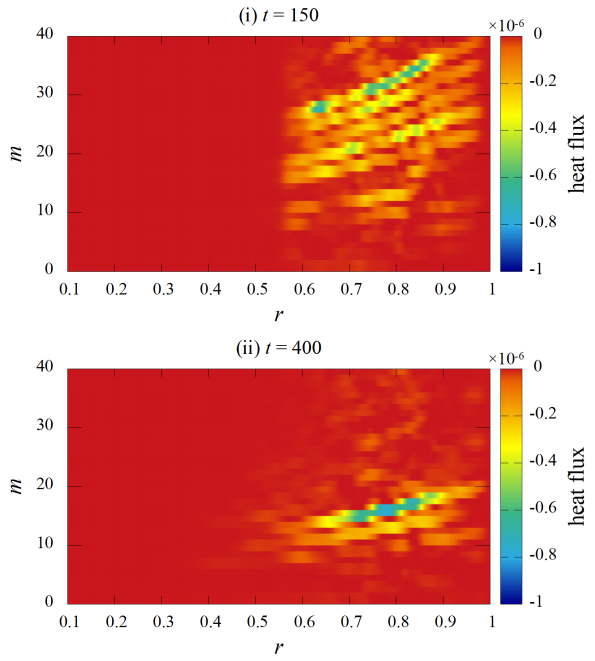

Fig. 10 Color contours of the convective heat flux spectrum $H^m_{\rm conv}(r)$ in r-m space for $\alpha = 0$ at (i) $t = 150$ and (ii) $t = 400$.

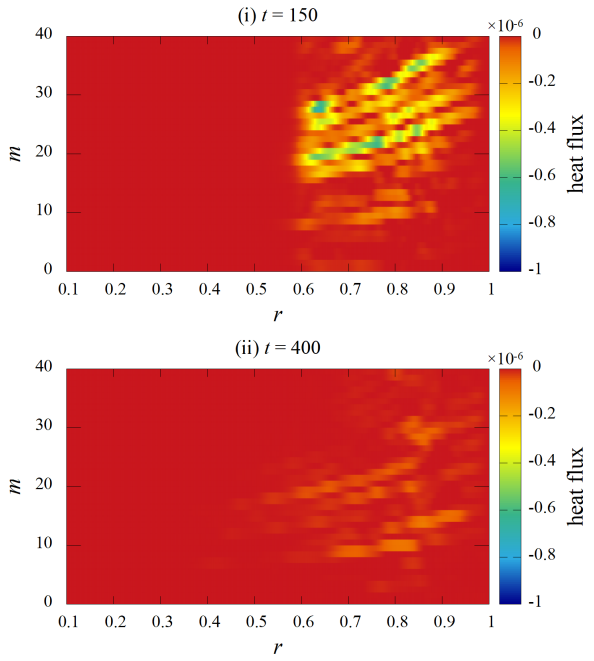

Fig. 11 Color contours of the convective heat flux spectrum $H^m_{\rm conv}(r)$ in r-m space for $\alpha = 1$ at (i) $t = 150$ and (ii) $t = 400$.

results in the reduction of the energy loss in Fig. 8. Comparing Figs. 9 (a) and 9 (b), it is observed that the contribution of the electromagnetic perturbation is negligible, and the contribution of the thermal diffusion tends to partially cancel out that of the convection.

Next, in order to decompose the convective heat flux into poloidal mode components, we use $H^m_{\rm conv}(r)$ defined by Eq. (32). Figure 10 shows the color contours of $H^m_{\rm conv}(r)$ in r-m space in the *absence* of the edge shear flow. In the beginning of the nonlinear phase at $t = 150$ (Fig. 10 (i)), it is observed that various modes contribute to the convective heat flux. On the other hand, in the phase of the radial turbulence spreading at $t = 400$ (Fig. 10 (ii)), contributions of the low-m modes are important, which is associated with the streamer structures in Fig. 4. Similarly, Fig. 11 shows the color contours of $H^m_{\rm conv}(r)$ in r-m space in the *presence* of the strong edge shear flow. Comparing Figs. 10 and 11, it is found that the convective heat flux spectrum is almost the same in both cases at $t = 150$, but the contributions of the low-m modes are less important in the case with the strong edge shear flow.

The results in Figs. 10 and 11 imply that the strong edge shear flow tends to avoid the inverse energy cascade in the mode number space. In order to verify this mechanism, we use E^m_p defined by Eq. (20). Figure 12 shows the poloidal mode number spectrum of the pressure perturbation energy in the phase of the radial turbulence spreading at $t = 400$. In the absence of the edge shear flow (Fig. 12 (a)), the peak in the range of $10 \lesssim |m| \lesssim 20$ is observed, which corresponds to the streamer structures in Fig. 4. On the other hand, such prominent peak in the

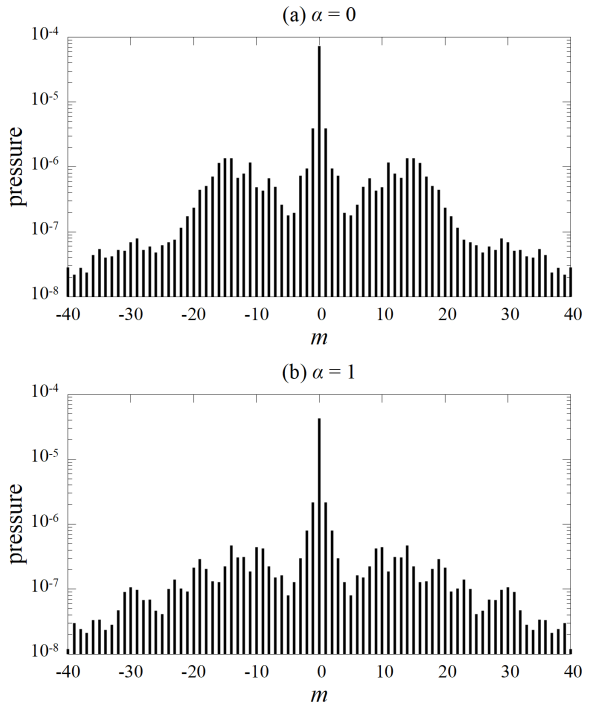

Fig. 12 Poloidal mode number spectrum of the pressure perturbation energy E^m_p for (a) $\alpha = 0$ and (b) $\alpha = 1$ at $t = 400$.

poloidal mode number space is absent in the case with the strong edge shear flow (Fig. 12 (b)).

4. Summary

In this study, we perform nonlinear simulations of

the ballooning mode turbulence using a reduced two-fluid model, and investigate how the edge shear flow affects the nonlinear evolution of the ballooning mode turbulence. In particular, from the perspective of the radial spreading of ballooning mode turbulence, the loss of the stored energy due to the ballooning mode turbulence is analyzed in detail. Based on the evolution equation of the change of the stored energy, a method to analyze the heat flux in the radial and mode number space is newly developed. Then, it becomes possible to quantitatively investigate the physical mechanism behind the relationship between the turbulence spreading and the edge shear flow.

In our simulation parameters, for the case without the equilibrium edge shear flow, the ballooning mode turbulence leads to the global heat transport by forming the secondary streamer structures. On the other hand, it is observed that, when the edge shear flow becomes stronger, such structures are not prominent and the global heat transport is suppressed. More specifically, it is found that the loss of stored energy roughly becomes half when the edge shear flow is as strong as the diamagnetic drift. Decomposing the heat flux into its components reveals that the convective heat transport is responsible for the global heat transport. Furthermore, by extracting the poloidal mode components that drive the convective heat transport, it is confirmed that global heat transport is mainly caused by the streamer structures. By comparing the time scale for the development of the streamer structures and the characteristic time scale of the edge shear flow, it is newly revealed that there is a physical mechanism that the edge shear flow prevents the formation of the streamer structures.

In the following, we compare our simulation results with the preceding works. It is shown in Ref. [8] that the radial spreading of the ballooning mode turbulence is suppressed by the edge shear flow. In this study, by analyzing the heat flux in the radial direction and mode number space, it is newly revealed that the edge shear flow suppresses not only the local convective heat transport but the global convective heat transport by affecting the secondary nonlinear evolution of the ballooning mode turbulence. In addition, the interaction between the spontaneously generated zonal flow and the ballooning mode turbulence in the absence of the equilibrium edge shear flow is investigated in Ref. [9]. Our simulation results imply that the formation of the zonal flow and its influence on the ballooning mode turbulence are less important in the presence of the strong equilibrium edge shear flow.

In this study, we neglect the ion diamagnetic drift, the parallel velocity, and the parallel thermal transport for simplicity, but those may affect the physics of the turbulence spreading. It is also important to consider a more realistic poloidal cross-section shape for better understanding of the ballooning mode turbulence in the advanced tokamaks. In our simulations, we use the relatively high resistivity. Therefore, it is also important to check how the choice of the resistivity affects the physical mechanism of the effect of the edge shear flow on the radial spreading of the ballooning mode turbulence. Those are left as future works.

Acknowledgments

The simulation code has been mainly developed using the facilities of the Center for Cooperative Work on Computational Science, University of Hyogo. We would like to acknowledge a Collaborative Research Program of Research Institute for Applied Mechanics, Kyushu University.

[1] G.T.A. Huijsmans, C.S. Chang, N. Ferraro, L. Sugiyama, F. Waelbroeck, X.Q. Xu, A. Loarte and S. Futatani, Phys. Plasmas **22**, 021805 (2015).
[2] J. Cheng, J.Q. Dong, K. Itoh, S.-I. Itoh, L.W. Yan, J.Q. Xu, M. Jiang, Z.H. Huang, K.J. Zhao, Z.B. Shi, W.L. Zhong, S. Inagaki, T. Kobayashi, K. Ida, Y. Kosuga, M. Sasaki, M.K. Han, Z.X. Wang, M. Xu, Y. Xu and HL-2A team, Nucl. Fusion **60**, 046021 (2020).
[3] M. Furukawa and S. Tokuda, Phys. Rev. Lett. **94**, 175001 (2005).
[4] N. Aiba, C. Giroud, M. Honda, E. Delabie, S. Saarelma, L. Frassinetti, I. Lupelli, F.J. Casson, S. Pamela, H. Urano, C.F. Maggi and JET Contributors, Nucl. Fusion **57**, 126001 (2017).
[5] C.K. Sun, X.Q. Xu, C.H. Ma and B. Li, Phys. Plasmas **25**, 082106 (2018).
[6] J.W. Connor, R.J. Hastie, H.R. Wilson and R.L. Miller, Phys. Plasmas **5**, 2687 (1998).
[7] X.Q. Xu, B.D. Dudson, P.B. Snyder, M.V. Umansky, H.R. Wilson and T. Casper, Nucl. Fusion **51**, 103040 (2011).
[8] P.W. Xi, X.Q. Xu, X.G. Wang and T.Y. Xia, Phys. Plasmas **19**, 092503 (2012).
[9] H. Seto, X.Q. Xu, B.D. Dudson and M. Yagi, Phys. Plasmas **26**, 052507 (2019).
[10] P. Beyer, S. Benkadda, G.F. Chaudier, X. Garbet, Ph. Ghendrih and Y. Sarazin, Plasma Phys. Control. Fusion **49**, 507 (2007).
[11] A. Thyagaraja, M. Valovič and P.J. Knight, Phys. Plasmas **17**, 042507 (2010).
[12] M. Leconte, P. Beyer, X. Garbet and S. Benkadda, Phys. Rev. Lett. **102**, 045006 (2009).
[13] S. Nishimura and M. Yagi, Plasma Fusion Res. **6**, 2403119 (2011).
[14] M. Bécoulet, F. Orain, G.T.A. Huijsmans, S. Pamela, P. Cahyna, M. Hoelzl, X. Garbet, E. Franck, E. Sonnendrücker, G. Dif-Pradalier, C. Passeron, G. Latu, J. Morales, E. Nardon, A. Fil, B. Nkonga, A. Ratnani and V. Grandgirard, Phys. Rev. Lett. **113**, 115001 (2014).
[15] D. Chandra, A. Thyagaraja, A. Sen and P. Kaw, Nucl. Fusion **57**, 076001 (2017).
[16] X. Garbet, L. Laurent, A. Samain and J. Chinardet, Nucl. Fusion **34**, 963 (1994).
[17] F. Hariri, V. Naulin, J.J. Rasmussen, G.S. Xu and N. Yan, Phys. Plasmas **23**, 052512 (2016).
[18] Y. Kosuga, S.-I. Itoh, P.H. Diamond and K. Itoh, Phys. Rev. E **95**, 031203(R) (2017).
[19] R.D. Hazeltine, M. Kotschenreuther and P.J. Morrison, Phys. Fluids **28**, 2466 (1985).